Illustrating the collaborative research on supercapacitors based on patronite−reduced graphene oxide hybrid headed by Dr Chandra Sekhar Rout at the School of Basic Sciences, IIT Bhubaneswar, India in collaboration with Prof. Saroj K. Nayak at the School of Basic Sciences, IIT Bhubaneswar, India, Dr Jogendra Nath Behera at the National Institute of Science Education and Research, India, Dr Nick Lanzillo at the Rensselaer Polytechnic Institute, USA and Dr. Stanislav Moshakalev at the State University of Campinas, Brazil.

Title: Supercapacitors based on patronite−reduced graphene oxide hybrids: experimental and theoretical insights

The electrochemical supercapacitive performance of the patronite−reduced graphene oxide hybrid was optimized by the synthesis conditions at three different concentrations. The experimental results were further corroborated by theoretical calculations.

As featured in:

See J. N. Behera, Chandra Sekhar Rout *et al.*, *J. Mater. Chem. A*, 2015, **3**, 18874.

ROYAL SOCIETY OF CHEMISTRY

www.rsc.org/MaterialsA

PAPER

Supercapacitors based on patronite–reduced graphene oxide hybrids: experimental and theoretical insights†

Satyajit Ratha,‡[a] Subba R. Marri,‡[b] Nicholas A. Lanzillo,[cd] Stanislav Moshkalev,[e] Saroj K. Nayak,[ac] J. N. Behera*[b] and Chandra Sekhar Rout*[a]

Here we report the hydrothermal synthesis and detailed study on supercapacitor applications of a patronite hybrid, VS_4/reduced graphene oxide, which showed an enhanced specific capacitance of ~877 F g^{-1} at a current density of 0.5 A g^{-1}. In comparison to bare vanadium sulfide and reduced graphene oxide, the hybrid showed ~6 times and ~5 times higher value of specific capacitance, respectively. The obtained energy density (117 W h kg^{-1}) and power density (20.65 kW kg^{-1}) are comparable to those of other reported transition metal sulfides and their graphene hybrids. Theoretical calculations using density functional theory confirm an enhanced quantum capacitance of VS_4/graphene composite systems, owing primarily to the shifting of the graphene Dirac cone relative to the band gap of VS_4. The results infer that the hybrid has the potential to be used as a high performance supercapacitor electrode.

1. Introduction

Recent developments in the field of two dimensional (2D) layered materials have drawn immense attention of researchers, globally. The intriguing properties exhibited by graphene in terms of its unmatched mechanical strength,[1–3] exceptionally high surface area,[4,5] high electrical and thermal conductivity[6,7] and resistance towards any kind of chemical adversity[8] have created a specific paradigm for it in the scientific community. In addition, there are other 2D inorganic graphene analogues like layered transition metal chalcogenides (TMCs) which are currently drawing significant attention due to their intricateness and tunable physical and chemical properties.[9–12] Because of their unique layered structures with each layer stacked onto another *via* weak van der Waals force, they can be easily exfoliated to form few layered structures.[13–15] Because of these properties, they have been known to form excellent materials to be used in flexible and transparent electronic devices.[16–18] Some of the TMCs like MoS_2, SnS_2, and WS_2 have been studied extensively owing to their exceptional applicability in areas like electronics,[18–20] energy storage,[21–24] energy conversion,[25–27] optoelectronics, *etc.*[22,28,29] TMCs have been extremely popular not only for their wide range of applications but also for the facile route by which they can be synthesized.[30,31] They have been studied in their pristine form as well as hybrid form with graphene/reduced graphene oxide (RGO).[24,29,32–35] Graphene/RGO as a platform provides mechanical support and facilitates fast charge transportation. In addition to that, hybrid structures comprising RGO, in most cases, result in formation of many active sites and tend to promote open edge growths, which greatly enhances their electrochemical and physical properties as compared to their pristine forms. A number of hybrid materials containing graphene/RGO as the active template have shown much improved performances.[33,36–38] For example, MoS_2/RGO has shown a much better specific capacitance value of 282 F g^{-1} as compared to 156 F g^{-1} for pristine MoS_2.[39] Similarly, WS_2/RGO showed a specific capacitance of 350 F g^{-1} which is 5 times higher as compared to bare WS_2.[24] Other metal sulfides such as NiS_2,[40,41] CoS_2,[41,42] FeS_2, *etc.*[43,44] have also been reported to show many intriguing applicabilities in various areas and it is highly expected that their graphene hybrids would yield even better results.

Vanadium sulfides are another prominent group of TMCs which have shown promising results in areas like energy storage,[45,46] sensing,[47] and spintronics.[48,49] Recently, few researchers have demonstrated that various stoichiometrically different forms of vanadium sulfides can be synthesized *via* facile hydrothermal routes.[50,51] Many interesting properties of vanadium sulfides have been explored recently. In their report,

[a] School of Basic Sciences, Indian Institute of Technology, Bhubaneswar 751013, India. E-mail: csrout@iitbbs.ac.in

[b] School of Chemical Sciences, National Institute of Science Education and Research (NISER), Bhubaneswar 751005, India. E-mail: jnbehera@niser.ac.in

[c] Department of Physics, Applied Physics, and Astronomy, Rensselaer Polytechnic Institute, Troy, New York 12180, USA

[d] Division of Science, Mathematics and Computing, Bard College, Annandale-on-Hudson, NY 12504, USA

[e] Center for Semiconductor Components, State University of Campinas, Campinas, Sao Paulo-13083-870, Brazil

† Electronic supplementary information (ESI) available. See DOI: 10.1039/c5ta03221k

‡ These authors contributed equally to this work.

Zhang *et al.* have shown that vanadium sulfide nano-ribbons have the potential to be used as an active material in spintronic devices.[48] The catalytic properties of vanadium sulfides have been detailed in a report by Guillard *et al.*[52] In another report, ultrathin nanosheets of VS_2 have shown exemplary moisture sensing properties.[47] Few layered flower-like VS_2 has been reported to have high field emission properties.[53] Jing *et al.* have conduced that 2D monolayered VS_2 has great potential as an anode material for Li-ion batteries.[46] Similarly, Feng *et al.* have inferred that VS_2 shows exceptional in-plane supercapacitor properties due to the correlation between electrons of vanadium atoms.[45] These reports suggest that vanadium sulfides do have the required physical and electrochemical properties to be used extensively in energy storage applications like supercapacitors and Li-ion batteries. Another such compound, VS_4, is currently under careful observation by a number of researchers due to its intriguing properties and unique morphology and composition. In VS_4, the vanadium atoms are present in an unusual geometry and form a linear chain containing two S_2^{2-} dimers, though the oxidation state of vanadium remains the same as in the case of VS_2. VS_4 mineral is known as patronite and was first discovered in the year 1906.[54] Its crystallographic data were specified in 1964,[55] and since then, many attempts have been made to synthesize it;[56–59] until recently, few reports depicted that it can be synthesized by a facile hydrothermal method in the presence of graphene as the template,[50,60,61] because graphene promotes the nucleation process which facilitates the growth of VS_4 instead of VS_2. VS_4/RGO is semiconducting in nature and possesses a band gap of the order 1.0 eV,[50] in contrast to VS_2 which is metallic. Also various reports reveal that it has potential applicability in the area of energy storage, especially the storage of lithium and it shows a much better reaction mechanism and high rate capacity.[61] It has also been reported that VS_4/RGO has excellent photocatalytic activity under visible-light irradiation.[60] Here we report the detailed supercapacitor performance of VS_4/RGO, synthesized by a facile one-step hydrothermal route and a thorough comparison with that of VS_2 and RGO.

2. Experimental methods

All the chemicals were used as supplied without any further modification.

2.1. Synthesis of GO and RGO

Graphene oxide (GO) was synthesized from graphite powder by a modified Hummer's method as detailed in an earlier report.[24] Further reduction of GO to form RGO was carried out by a hydrothermal reaction performed at 160 °C for 24 h.

2.2. Synthesis of VS_2 and VS_4/RGO

VS_2 sheets were synthesized by a previously reported hydrothermal method involving the reaction of sodium orthovanadate (Na_3VO_4, Sigma-Aldrich, 99.98%) and thioacetamide (C_2H_5NS, Sigma-Aldrich, ≥99%) at 160 °C.[50,53] During the hydrothermal reaction, hydrolysis of thioacetamide generates

HS^-, which acts as a reductant to reduce V^{5+} into V^{4+} and VS_2 layered structures are formed. VS_4 sheets were also synthesized by the same hydrothermal reaction in a GO solution (with varied GO concentrations) at 160 °C and the final carbon content of the composite was estimated by elemental analysis.[50,53] During the hydrothermal process, VS_4 sheets were formed on GO and the GO transformed to RGO.[50]

2.3. Characterization

The samples were characterized by X-ray diffraction (Bruker D8 Advance diffractometer, 40 kV, 40 mA) having Ni filtered Cu-K_α radiation with a wavelength, $\lambda = 1.54184$ Å. Morphology of the sample was studied by FESEM (Merlin Compact with GEMINI-I column, Zeiss Pvt. Ltd, Germany). EDAX and elemental mapping (INCA, Oxford Instruments, UK) were also performed. Raman spectroscopy was performed using a micro Raman spectrometer (Renishaw inVia Raman microscope).

2.4. Electrochemical measurement

2.4.1. Two electrode measurement. The electrochemical supercapacitor properties of the samples were tested with the help of Swagelok type two electrode cells comprising high grade stainless steel electrodes with Teflon encapsulation. The stainless steel electrodes were polished with emery paper and alumina powder (1 μm Al_2O_3) for about 30 minutes and then sonicated with de-ionized (DI) water for about 1 h. In a typical procedure, 4 mg of the sample was taken and it was finely ground with the help of a mortar-pestle for about 1–2 h. Then, it was equally divided and was taken in two different glass tubes and dispersed with a viable amount of ethanol by ultra-sonication in an ice bath for about 15 minutes in order to achieve a nearly homogeneous mixture containing ethanol and the sample. The sample contained in one glass tube was drop-cast onto one electrode using a micropipette so that each electrode would carry 2 mg of the sample with uniform coverage. Both the electrodes were then dried in a vacuum desiccator for about 2–3 h. To provide separation between these electrodes, a porous cellulose nitrate membrane (Himedia Laboratories, Pvt. Ltd, India) having diameter equal to the diameter of the electrodes and pore size ~0.22 μm was used. Before that, the membrane was thoroughly soaked in 1 M aqueous Na_2SO_4 solution which acted as the electrolyte. All the measurements like cyclic voltammetry (CV) at different scan rates, charge–discharge (CD) at different current densities and long cycle stability test were performed by using a potentiostat/galvanostat (PG262A, Techno science Ltd, Bangalore, India) while keeping the working potential within the range of −0.1 V to 0.9 V.

2.4.2. Three electrode measurement. Investigation and comparison of the redox (faradic) activities of VS_2 and VS_4/RGO have been carried out using a three-electrode electrochemical configuration. For that, a typical glassy carbon electrode (GCE) coated with the sample was used as the working electrode, Ag/AgCl was taken as the reference electrode and a platinum wire was used as the counter electrode. First, the GCE was properly polished with fine emery paper and alumina powder (0.3 μm Al_2O_3) for about 10–15 minutes and then sonicated in DI water

for 30 minutes and dried in a vacuum desiccator for 1 h. About 1 mg of the sample was dispersed in 100 μl of ethanol to get a homogeneous mixture and then 2.5 μl of the homogeneous mixture was drop-casted onto the mirror finished surface of the GCE using a micropipette. 5 μl of nafion was then drop-coated onto the as deposited sample and was kept in a vacuum desiccator, overnight. Cyclic voltammetry at a particular scan rate (10 mV s^{-1}) was performed by taking 1 M aqueous Na$_2$SO$_4$ solution as the electrolyte to verify the pseudocapacitive (in terms of faradic reaction) behavior of VS$_2$ and VS$_4$/RGO. Here the working potential range was kept within −0.1 V to 0.9 V.

2.5. Calculation of specific capacitance, power density and energy density

All the calculations such as specific capacitance, energy density, and power density were performed by taking the data from two-electrode measurements. Specific capacitance of the sample was calculated from both the cyclic voltammetry and charge–discharge curves. From the cyclic voltammetry curves, the specific capacitance was calculated using the following equation:[62]

$$C_{sp}^{CV} = \frac{\oint I(V)dV}{mr \times 2(V_f - V_i)} = \frac{\int_{-0.1}^{0.9} I(V)dV + \int_{0.9}^{-0.1} I(V)dV}{mr \times 2(V_f - V_i)} \quad (1)$$

where C_{sp}^{CV} is the specific capacitance calculated using CV curves, m is the mass of the sample drop-cast on one electrode (2 mg), r is the scan rate, $V_f - V_i$ is the potential window ($V_f = 0.9$ V and $V_i = -0.1$ V) and $I(V)dV$ is the area under the cyclic voltammetry curve. Similarly, the specific capacitance from the charge–discharge curves was calculated using the following equation:

$$C_{sp}^{cd} = \frac{I}{ms} \quad (2)$$

where C_{sp}^{cd} is specific capacitance calculated using charge–discharge curves, s is the slope of the discharge curve, and I is the current at which the charge–discharge measurement was performed.

The energy density (E_d) of the sample was calculated from the cyclic voltammetry data by using the following equation:

$$E_d = \frac{1}{2} C_{sp}^{CV} (V_f - V_i)^2 \quad (3)$$

The unit here is J g^{-1} which is why eqn (3) should be divided by a factor of 3600 to get the unit converted to W h g^{-1}. To obtain E_d in terms of W h kg^{-1}, the modified equation was again multiplied by a factor of 1000, as given below:

$$E_d = \frac{1}{2} \frac{1000}{3600} C_{sp}^{CV} (V_f - V_i)^2 \quad (4)$$

Power density (P_d) from the CV curve was calculated using eqn (5), as given below:

$$P_d = \frac{1}{2} C_{sp}^{CV} (V_f - V_i)r \quad (5)$$

where r is the rate of scan at which the CV measurement was performed. Here the working potential window (i.e. $V_f - V_i$) is of the same value as taken for the evaluation of specific capacitance using eqn (1).

3. Results and discussion

VS$_4$/RGO containing 0.75 wt% of RGO, 1.5 wt% of RGO and 3 wt% of RGO have been denoted hereafter as VS$_4$/RGO_0.75, VS$_4$/RGO_1.5 and VS$_4$/RGO_3, respectively. FESEM images of the VS$_4$/RGO (1.5%) hybrid confirm uniform distribution of VS$_4$ over the RGO layer (Fig. 1a and b). Fig. 1c shows the EDS data of the VS$_4$/RGO hybrid confirming the presence of the components with appropriate proportions. Elemental mapping of the hybrid has also been carried out (Fig. 2a–d) depicting the uniformity of the elements in the hybrid. Fig. 2e shows the X-ray diffraction pattern of the hybrid demonstrating a prominent growth along the (110) direction with another peak along (020). FESEM and XRD analyses of pristine VS$_2$ confirm the formation of a pure phase without any impurity (see Fig. S1 in the ESI†). In the XRD pattern of VS$_4$/RGO, the suppressed carbon peak (at 2θ value of ∼26°), characteristic of RGO, is due to the low thickness of the RGO layer and the sharp crystalline peak of VS$_4$. Applying the Scherrer equation (to calculate the crystallite size over all FWHM values of diffraction peaks), the average grain size was found to be within the range of 24–29 nm. It confirms the uniformity of the VS$_4$ crystallites in the hybrid. All these diffraction peaks can be assigned to a highly crystalline patronite V(S$_2$)$_2$ having a monoclinic structure (JCPDS file: 72-1294). Furthermore, the diffraction patterns of VS$_4$/RGO_0.75 and VS$_4$/RGO_3 were compared with that of VS$_4$/RGO_1.5 (see Fig. S2a in the ESI†). The hybrid containing 0.75 wt% of RGO shows poor uniformity of the VS$_4$ crystallites (hence larger grain boundaries) and also has additional peak of VS$_2$ (along the direction of (004), denoted by the asterisk mark in Fig. S2a†) which may be due to the insufficiency of the RGO template which hindered the nucleation of VS$_4$ significantly. However, better crystallinity of VS$_4$ is clearly visible in the case of both VS$_4$/RGO_1.5 and VS$_4$/RGO_3. To check the reduction quality of GO in the case of RGO and the hybrid, X-ray photoelectron spectroscopy has been performed (see Fig. S2b in the ESI†). The characteristic C1s spectra of all the three samples were compared. As can be seen, the C1s spectrum of GO has two distinct peaks at 285 eV (C–C) and 289.48 (O–C=O). Whereas for RGO and the hybrid, only one distinct peak is observed at 284.48 eV (C–C) indicating the absence of oxygen containing functional groups (due to the thermal reduction process). Raman spectroscopy for GO, RGO and VS$_4$/RGO was performed to investigate the vibrational modes and the quality of reduction of GO in both RGO sample and the hybrid. Fig. S2c† shows the Raman spectra of the samples. It shows the characteristic D and G bands for both GO and RGO. The D-band appears at ∼1350 cm^{-1} which confirms lattice distortions and the G-band appears at ∼1590 cm^{-1} which corresponds to the first order scattering (E$_{2g}$ mode).[63] The I_D/I_G ratio of GO, bare RGO and RGO in the hybrid has also been calculated. The increased intensity ratio in the case of both bare RGO and RGO present in the hybrid is in

good agreement with previously reported data.[63,64] It confirms the restoration of sp^2 carbons and formation of smaller sp^2 domains. The electrochemical measurements were performed for VS_2, RGO and VS_4/RGO at three different concentrations (*i.e.* 0.75 wt%, 1.5 wt% and 3 wt%) of RGO. Fig. 3a and c show the cyclic voltammetry and charge–discharge curves of the VS_4/RGO_1.5 hybrid using a two-electrode system. At a scan rate of 2 mV s^{-1}, it showed a specific capacitance of 845 F g^{-1}. This high value of specific capacitance can be attributed to the electric double layer capacitance (EDLC) from the RGO layer as well as pseudocapacitive contribution from VS_4. Electrochemical measurements (using two-electrode configuration) were also carried out for pristine VS_2 (Fig. S3†), RGO (Fig. S4†), VS_4/RGO_0.75 (Fig. S5†) and VS_4/RGO_3 (Fig. S6†). Comparison between the supercapacitor performances of VS_4/RGO_1.5, RGO and VS_2 is elucidated in Table 2. Dependence of specific capacitance on both scan rates and current densities is shown in Fig. 3b and d, respectively. At a current density of 0.5 A g^{-1}, the hybrid shows its maximum calculated specific capacitance of 877 F g^{-1}. The obtained specific capacitance of the VS_4/RGO hybrid is found to be comparable to that of the best supercapacitors based on other metal sulfides reported in the literature (see Table 1). For example, NiS nanoparticles on graphene oxide sheets grown by a facile hydrothermal route have shown a specific capacitance of 800 F g^{-1} at a current density of 1 A g^{-1}.[65] Wang *et al.*,[66] have reported supercapacitors based on Co_3S_4 hollow nanospheres on graphene which showed a maximum specific capacitance of ~675 F g^{-1}. At higher scan rates, the capacitance values decrease as shown in Fig. 3b. The phenomenon can be correlated with a kinetically slow faradic reaction on the electrode surface and high electrolytic resistance (slower response towards voltage changes during fast scan). For higher scan rates, the cycle completes with a lower value of the surface reaction and the resultant current (including the much lower value of faradic current) is mostly due to the double layer capacitive properties of the hybrid. This does not occur with lower scan rates, resulting in the decrease in capacitance value as the scan rate increases. The values of specific capacitance for the hybrid obtained at different current densities are comparable to the values obtained at different scan rates. Also the charge–discharge curves are nearly symmetrical which explains that the redox reaction (faradic reaction) is reversible in nature and the material possesses good capacitive properties. Further, it was found that VS_4/RGO_1.5 shows much better capacitive effect as compared to both VS_4/RGO_0.75 and VS_4/RGO_3. In the case of VS_4/RGO_0.75, the reason behind poor electrochemical performance is due to the large variation in the grain size of VS_4 particles and their non-uniform distribution on the RGO layer. As the concentration of RGO was not optimum, the nucleation of VS_4 was not facilitated in a significant manner (which can be inferred from additional VS_2 peaks found in the X-ray diffraction pattern of VS_4/RGO_0.75 which is shown in Fig. S2a† by the asterisk mark). Although better electrochemical performance should have been shown by VS_4/RGO_3, the undesired outcome may be assigned to the agglomeration of VS_4 particles and RGO to form larger entities due to the uncontrolled nucleation process in the presence of RGO at an
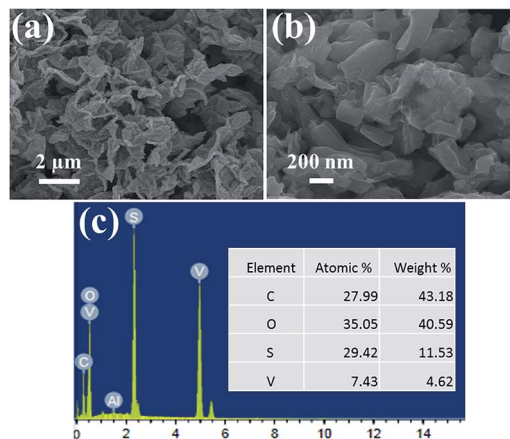

Fig. 1 (a) Low and (b) high magnification FESEM images of the VS_4/RGO_1.5 hybrid. (c) EDS spectrum, atomic percentage and weight percentage of the elements.

excess concentration.[67] This agglomeration effect was avoided in the hybrid with 1.5 wt% of RGO in which the coordination between VS_4 and RGO was superior, which yielded better electrochemical supercapacitor performances. This was further corroborated by the detailed electrochemical investigation carried out for VS_4/RGO_0.75, VS_4/RGO_1.5 and VS_4/RGO_3 in this report. Thus the capacitive effect of the hybrid has a strong dependency on the RGO concentration. Fig. 4a shows the Ragone plot which depicts the energy density and power density
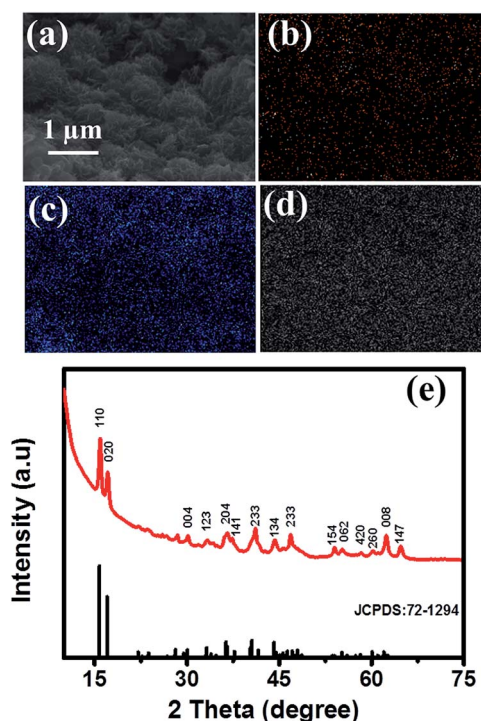

Fig. 2 Elemental analysis of VS_4/RGO_1.5. (a) Electron image of the hybrid over which the mapping has been performed. Presence of (b) carbon, (c) sulfur and (d) vanadium in the hybrid. (e) XRD pattern of VS_4/RGO_1.5 showing prominent growth along (110).
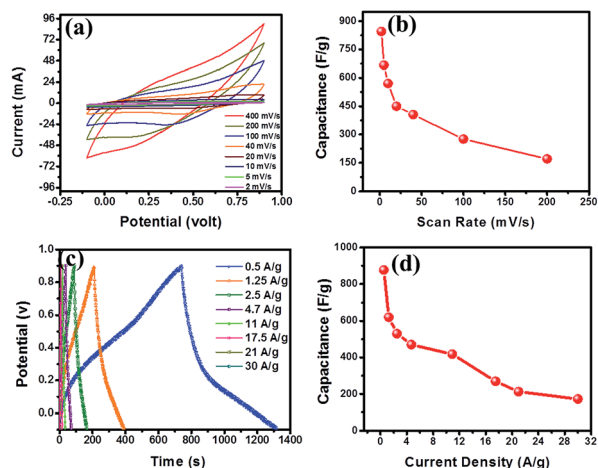
Fig. 3 Two-electrode measurement data of VS$_4$/RGO_1.5. (a) Cyclic voltammetry curves at different scan rates and (b) specific capacitance vs. scan rate showing a gradual decrease in capacitance at higher scan rates. (c) Charge–discharge curves at different current densities and (d) variation of capacitance with current density.

of the hybrid material at different scan rates. At a scan rate of 2 mV s^{-1}, the hybrid material shows a maximum energy density of the order of ~117 W h kg^{-1} and a maximum power density of the order of ~20.65 kW kg^{-1}. Stability is a factor of immense priority for the material, which is to be used as a supercapacitor electrode and therefore a long cycle charge–discharge measurement was performed in which the stability of the hybrid was tested for about 1000 cycles. Fig. 4b shows the last 5 cycles of the long cyclic measurement, carried out at a current density of 9 A g^{-1}. The specific capacitance value of the hybrid was calculated at an interval of 50 cycles and the corresponding plot is provided in Fig. 4c and the inset shows the data containing 1000 cycles of charge–discharge. The data shown in Fig. 4c elucidate that even after 1000 cycles the degradation in specific capacitance of the hybrid material is merely ~10% of the initial value. The corresponding Ragoneplots of VS$_4$/RGO_0.75, VS$_4$/RGO_3, VS$_2$ and RGO are provided in Fig. S7.† VS$_2$ is metallic whereas VS$_4$ is a low band gap semiconductor with superior electrochemical properties. Comparative electrochemical cyclic voltammograms are shown in Fig. S8† which illustrates the redox activity of both VS$_2$ and VS$_4$ (VS$_4$/RGO) at a scan rate of 5 mV s^{-1}. It can be observed that the pseudocapacitive behaviour of VS$_4$ in the hybrid is better than that of pristine VS$_2$. The reason behind such an anomaly can be

correlated with the defect parameters (in terms of functional groups such as carbonyl, epoxy or hydroxyl, etc.) already present in RGO layers, which readily contribute towards the surface faradic reaction making the redox activity of VS$_4$/RGO more prominent as compared to that of bare VS$_2$.

3.1. Computational results

Density-functional simulations were performed using the SIESTA[68] software package to investigate the electronic structure of the graphene/VS$_4$ interface. The details are reported in the ESI.† A side image of the 1-dimensional "chains" that make up bulk VS$_4$ is shown in Fig. 5a with adjacent chains extending in the direction perpendicular to the page. The interaction between adjacent chains as well as between the chains and graphene is weak and due to the van der Waals interaction.[50] We considered a single monolayer of these chains spaced 3.3 Å above a graphene sheet, with the spacing between adjacent chains taken to be the same as in the bulk structure. The
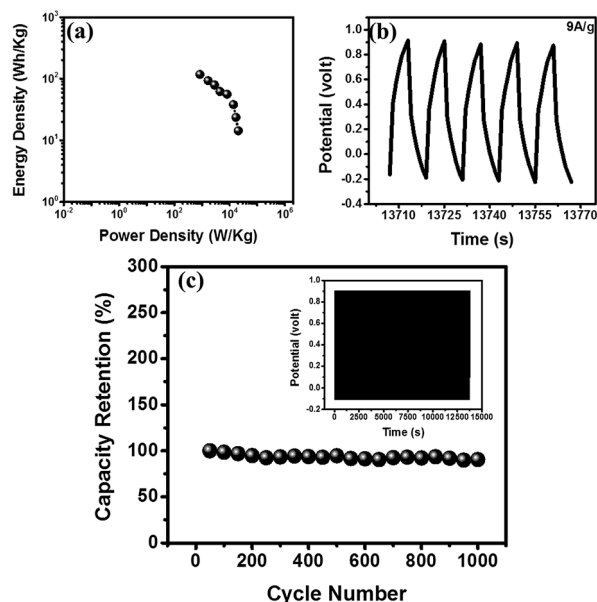

Fig. 4 (a) Power density and energy density of VS$_4$/RGO_1.5 at different current densities, and (b) last 5 cycles taken from the long cycle stability test to show no variation of symmetry in the charge–discharge pattern even after 1000 cycles. (c) Capacity retention of the hybrid showing much better stability even after 1000 cycles with the inset showing the data plot for 1000 charge–discharge cycles.

Table 1 Comparison of supercapacitor performance of VS$_4$/RGO_1.5 with the reported metal sulfides/graphene hybrids

Hybrid	Maximum specific capacitance	Maximum energy density	Maximum power density	Reference
NiS/graphene	775 F g^{-1} (at 0.5 A g^{-1})	11.2 W h kg^{-1}	~1 kW kg^{-1}	69
WS$_2$/RGO	350 F g^{-1} (at 2 mV s^{-1})	49 W h kg^{-1}	8.2 kW kg^{-1}	24
Co$_3$S$_4$/graphene	675.9 F g^{-1} (at 0.5 A g^{-1})	—	—	66
CoS$_2$/graphene	314 F g^{-1} (0.5 A g^{-1})	—	—	70
VS$_4$/RGO_1.5	877 F g^{-1} (at 0.5 A g^{-1})	117 W h kg^{-1}	20.65 W kg^{-1}	Present work

18878 | J. Mater. Chem. A, 2015, 3, 18874–18881

This journal is © The Royal Society of Chemistry 2015

Table 2   Comparison of supercapacitor performance of $VS_4/RGO\_0.75$, $VS_4/RGO\_1.5$, VS_4/RGO_3, RGO and VS_2

Sample	Maximum specific capacitance	Maximum energy density	Maximum power density
$VS_4/RGO\_0.75$	223 F g^{-1}	29.72 W h kg^{-1}	4.53 kW kg^{-1}
$VS_4/RGO\_1.5$	877 F g^{-1}	117 W h kg^{-1}	20.65 kW kg^{-1}
VS_4/RGO_3	259 F g^{-1}	35.36 W h kg^{-1}	11.57 kW kg^{-1}
RGO	144 F g^{-1}	20 W h kg^{-1}	6.2 kW kg^{-1}
VS_2	137 F g^{-1}	19 W h kg^{-1}	6 W kg^{-1}

monolayer was cut in the direction indicated by the red arrow in Fig. 5a and the resulting structure is shown in Fig. 5b.

The quantum capacitance C_q is related to the density of states $g(\varepsilon)$ through the following relationship:

$$C_q = \frac{e^2}{4k_BT} \int_{-\infty}^{\infty} d\varepsilon g(\varepsilon) \text{sech}^2\left(\frac{\varepsilon - \mu}{2k_BT}\right) \quad (6)$$

where e is the fundamental electronic charge, k_B is the Boltzmann's constant, T is the temperature (taken to be 300 K here) and μ is the Fermi Energy. The calculated density-of-states for the graphene/VS_4 interface is shown in Fig. 5c, where both the Dirac cone of graphene and the band gap of VS_4 are clearly visible below and above the Fermi level, respectively. Interestingly, because the Dirac cone of graphene is not located inside the band gap of VS_4, the net DOS gives rise to a larger-than-expected quantum capacitance in this region (Fig. 5d). The shape of the capacitance with respect to the bias potential mirrors that of the density of states near the Fermi level. For all values of bias voltage considered, the quantum capacitance of the composite graphene/VS_4 system is larger than that of graphene alone, a trend that confirms the measured experimental capacitance. It is worth noting that the quantum capacitance of a semiconductor in the off state is defined to be zero.

Depending on the bias voltage considered, the capacitance of the composite system is anywhere from roughly 1 to 10 times larger than that of graphene alone.

4.   Conclusions

The synthesis of the VS_4/RGO hybrid by a facile one-step hydrothermal technique has been accomplished and its supercapacitor performance is tested. The results obtained so far have shown great potential of the VS_4/RGO hybrid with specific capacitance as high as 877 F g^{-1}. Simulations based on density functional theory confirm an enhanced quantum capacitance when VS_4 is heterostructured with graphene, primarily due to the location of the graphene Dirac cone relative to the band gap of VS_4. The hybrids exhibited an enhanced energy density of ~117 W h kg^{-1} and a power density of ~20 kW kg^{-1} which are compared to those of reported metal sulfides and their graphene based hybrids. These experimental and theoretical findings provide useful insights into the design of supercapacitors for potential high performance energy storage application in the future.

Acknowledgements

Fig. 5   (a) Side-view of the one-dimensional chains that make up bulk VS_4. (b) The graphene/VS_4 interface used for the simulations, (c) density of states of the graphene/VS_4 heterostructure and (d) quantum capacitance for the graphene/VS_4 interface.

Notes and references

1 Z. Ni, H. Bu, M. Zou, H. Yi, K. Bi and Y. Chen, *Phys. Rev. B: Condens. Matter Mater. Phys.*, 2010, **405**, 1301–1306.
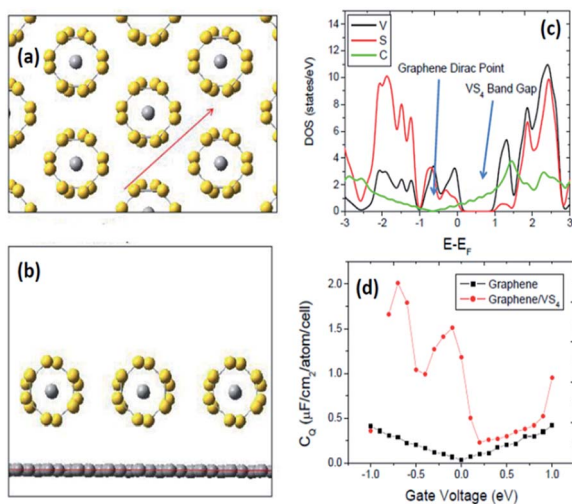2 N. Ferralis, *J. Mater. Sci.*, 2010, **45**, 5135–5149.

3 A. H. Castro Neto, N. M. R. Peres, K. S. Novoselov and A. K. Geim, *Rev. Mod. Phys.*, 2009, **81**, 109–162.

4 A. K. Geim, *Science*, 2009, **324**, 1530–1534.

5 X. Li, W. Cai, J. An, S. Kim, J. Nah, D. Yang, R. Piner, A. Velamakanni, I. Jung, E. Tutuc, S. K. Banerjee, L. Colombo and R. S. Ruoff, *Science*, 2009, **324**, 1312–1314.

6 S. Stankovich, D. A. Dikin, G. H. B. Dommett, K. M. Kohlhaas, E. J. Zimney, E. A. Stach, R. D. Piner, S. T. Nguyen and R. S. Ruoff, *Nature*, 2006, **442**, 282–286.

7 A. K. Geim and K. S. Novoselov, *Nat. Mater.*, 2007, **6**, 183–191.

8 P. Blake, P. D. Brimicombe, R. R. Nair, T. J. Booth, D. Jiang, F. Schedin, L. A. Ponomarenko, S. V Morozov, H. F. Gleeson, E. W. Hill, A. K. Geim and K. S. Novoselov, *Nano Lett.*, 2008, **8**, 1704–1708.

9 G. Chatzitheodorou, S. Fiechter, M. Kunst, J. Luck and H. Tributsch, *Mater. Res. Bull.*, 1988, **23**, 1261–1271.

10 M.-R. Gao, J. Jiang and S.-H. Yu, *Small*, 2012, **8**, 13–27.

11 P. Johari and V. B. Shenoy, *ACS Nano*, 2012, **6**, 5449–5456.

12 R. Lv, J. a. Robinson, R. E. Schaak, D. Sun, Y. Sun, T. E. Mallouk and M. Terrones, *Acc. Chem. Res.*, 2014, **48**, 56–64.

13 X. Zhang, F. Meng, J. R. Christianson, C. Arroyo-Torres, M. A. Lukowski, D. Liang, J. R. Schmidt and S. Jin, *Nano Lett.*, 2014, **14**, 3047–3054.

14 J. H. Han, S. Lee and J. Cheon, *Chem. Soc. Rev.*, 2013, **42**, 2581–2591.

15 H. Fang, C. Battaglia, C. Carraro, S. Nemsak, B. Ozdol, J. S. Kang, H. A. Bechtel, S. B. Desai, F. Kronast, A. A. Unal, G. Conti, C. Conlon, G. K. Palsson, M. C. Martin, A. M. Minor, C. S. Fadley, E. Yablonovitch, R. Maboudian and A. Javey, *Proc. Natl. Acad. Sci. U. S. A.*, 2014, **111**, 6198–6202.

16 R. Gatensby, N. McEvoy, K. Lee, T. Hallam, N. C. Berner, E. Rezvani, S. Winters, M. O'Brien and G. S. Duesberg, *Appl. Surf. Sci.*, 2014, **297**, 139–146.

17 Y. Zhang, J. Ye, Y. Matsuhashi and Y. Iwasa, *Nano Lett.*, 2012, **12**, 1136–1140.

18 J. Wang, X. Zou, X. Xiao, L. Xu, C. Wang, C. Jiang, J. C. Ho, T. Wang, J. Li and L. Liao, *Small*, 2014, 208–213.

19 H. T. Yuan, M. Toh, K. Morimoto, W. Tan, F. Wei, H. Shimotani, C. Kloc and Y. Iwasa, *Appl. Phys. Lett.*, 2011, **98**, 012102.

20 W. Sik Hwang, M. Remskar, R. Yan, V. Protasenko, K. Tahy, S. Doo Chae, P. Zhao, A. Konar, H. Xing, A. Seabaugh and D. Jena, *Appl. Phys. Lett.*, 2012, **101**, 013107.

21 Y. Yang, H. Fei, G. Ruan, C. Xiang and J. M. Tour, *Adv. Mater.*, 2014, **26**, 8163–8168.

22 H. X. Zhong, G. Z. Yang, H. W. Song, Q. Y. Liao, H. Cui, P. K. Shen and C. X. Wang, *J. Phys. Chem. C*, 2012, **116**, 9319–9326.

23 R. Bhandavat, L. David and G. Singh, *J. Phys. Chem. Lett.*, 2012, **3**, 1523–1530.

24 S. Ratha and C. S. Rout, *ACS Appl. Mater. Interfaces*, 2013, **5**, 11427–11433.

25 T. Wang, D. Gao, J. Zhuo, Z. Zhu, P. Papakonstantinou, Y. Li and M. Li, *Chem.–Eur. J.*, 2013, **19**, 11939–11948.

26 B. Yang, Z. Xu, H. Yu, Z.-G. Chen and L. Wang, *Chem.–Eur. J.*, 2014, **20**, 8670–8676.

27 K. Ellmer, *Phys. Status Solidi*, 2008, **245**, 1745–1760.

28 D.-S. Tsai, K.-K. Liu, D.-H. Lien, M.-L. Tsai, C.-F. Kang, C.-A. Lin, L.-J. Li and J.-H. He, *ACS Nano*, 2013, **7**, 3905–3911.

29 S. Ratha, A. J. Simbeck, D. J. Late, S. K. Nayak and C. S. Rout, *Appl. Phys. Lett.*, 2014, **105**, 243502.

30 S. Ding, D. Zhang, J. S. Chen and X. W. Lou, *Nanoscale*, 2012, **4**, 95–98.

31 Y. Lei, S. Song, W. Fan, Y. Xing and H. Zhang, *J. Phys. Chem. C*, 2009, **113**, 1280–1285.

32 L. David, R. Bhandavat and G. Singh, *ACS Nano*, 2014, **8**, 1759–1770.

33 K. Roy, M. Padmanabhan, S. Goswami, T. P. Sai, G. Ramalingam, S. Raghavan and A. Ghosh, *Nat. Nanotechnol.*, 2013, **8**, 826–830.

34 C. S. Rout, P. D. Joshi, R. V. Kashid, D. S. Joag, M. A. More, A. J. Simbeck, M. Washington, S. K. Nayak and D. J. Late, *Appl. Phys. Lett.*, 2014, **105**, 43109.

35 M. Sathish, S. Mitani, T. Tomai and I. Honma, *J. Phys. Chem. C*, 2012, **116**, 12475–12481.

36 D. Wang, D. Choi, J. Li, Z. Yang, Z. Nie, R. Kou, D. Hu, C. Wang, L. V. Saraf, J. Zhang, I. A. Aksay and J. Liu, *ACS Nano*, 2009, **3**, 907–914.

37 G. Xiong, K. P. S. S. Hembram, R. G. Reifenberger and T. S. Fisher, *J. Power Sources*, 2013, **227**, 254–259.

38 M. Khalid, M. A. Tumelero, V. C. Zoldan, C. C. Pla Cid, D. F. Franceschini, R. A. Timm, L. T. Kubota, S. A. Moshkalev and A. A. Pasa, *RSC Adv.*, 2014, **4**, 34168–34178.

39 S. Patil, A. Harle, S. Sathaye and K. Patil, *CrystEngComm*, 2014, **16**, 10845–10855.

40 H. Pang, C. Wei, X. Li, G. Li, Y. Ma, S. Li, J. Chen and J. Zhang, *Sci. Rep.*, 2014, **4**, 3577.

41 S. Peng, L. Li, H. Tan, R. Cai, W. Shi, C. Li, S. G. Mhaisalkar, M. Srinivasan, S. Ramakrishna and Q. Yan, *Adv. Funct. Mater.*, 2014, **24**, 2155–2162.

42 S. Amaresh, K. Karthikeyan, I.-C. Jang and Y. S. Lee, *J. Mater. Chem. A*, 2014, **2**, 11099–11106.

43 J. Xu, H. Xue, X. Yang, H. Wei, W. Li, Z. Li, W. Zhang and C.-S. Lee, *Small*, 2014, **10**, 4754–4759.

44 J. Puthussery, S. Seefeld, N. Berry, M. Gibbs and M. Law, *J. Am. Chem. Soc.*, 2010, **133**, 716–719.

45 J. Feng, X. Sun, C. Wu, L. Peng, C. Lin, S. Hu, J. Yang and Y. Xie, *J. Am. Chem. Soc.*, 2011, **133**, 17832–17838.

46 Y. Jing, Z. Zhou, C. R. Cabrera and Z. Chen, *J. Phys. Chem. C*, 2013, **117**, 25409–25413.

47 J. Feng, L. Peng, C. Wu, X. Sun, S. Hu, C. Lin, J. Dai, J. Yang and Y. Xie, *Adv. Mater.*, 2012, **24**, 1969–1974.

48 Y. Zhang and X. Wu, *Phys. Lett. A*, 2013, **377**, 3154–3157.

49 Y. Ma, Y. Dai, M. Guo, C. Niu, Y. Zhu and B. Huang, *ACS Nano*, 2012, **6**, 1695–1701.

50 C. S. Rout, B.-H. Kim, X. Xu, J. Yang, H. Y. Jeong, D. Odkhuu, N. Park, J. Cho and H. S. Shin, *J. Am. Chem. Soc.*, 2013, **135**, 8720–8725.

51 C. Q. Song, K. Yu, H. H. Yin, H. Fu, Z. L. Zhang, N. Zhang and Z. Q. Zhu, *J. Mater. Chem. C*, 2014, **2**, 4196–4202.

52 C. Guillard, M. Lacroix, M. Vrinat, M. Breysse, B. Mocaer, J. Grimblot, T. des Courieres and D. Faure, *Catal. Today*, 1990, **7**, 587–600.

53 C. S. Rout, R. Khare, R. V Kashid, D. S. Joag, M. A. More, N. A. Lanzillo, M. Washington, S. K. Nayak and D. J. Late, *Eur. J. Inorg. Chem.*, 2014, 5331–5336.

54 W. F. Hillebrand, *J. Am. Chem. Soc.*, 1907, **29**, 1019–1029.

55 Patronite Miner, Data. Mineral. database, http//www.webmineral.com/data/Patronite.shtml.

56 M. Yokoyama, M. Yoshimura, M. Wakihara, S. Somiya and M. Taniguchi, *J. Solid State Chem.*, 1985, **60**, 182–187.

57 M. Nakano-Onoda, S. Yamaoka, K. Yukino, K. Kato and I. Kawada, *J. Less-Common Met.*, 1976, **44**, 341–344.

58 M. Taniguchi, M. Wakihara and Y. Shirai, *Z. Anorg. Allg. Chem.*, 1980, **461**, 234–240.

59 T. Murugesan, S. Ramesh, J. Gopalakrishnan and C. N. R. Rao, *J. Solid State Chem.*, 1982, **44**, 119–125.

60 W. Guo and D. Wu, *Int. J. Hydrogen Energy*, 2014, **39**, 16832–16840.

61 X. Xu, S. Jeong, C. S. Rout, P. Oh, M. Ko, H. Kim, M. G. Kim, R. Cao, H. S. Shin and J. Cho, *J. Mater. Chem. A*, 2014, **2**, 10847–10853.

62 S. Zhang and N. Pan, *Adv. Energy Mater.*, 2015, **5**, 1401401.

63 S. Stankovich, D. A. Dikin, R. D. Piner, K. A. Kohlhaas, A. Kleinhammes, Y. Jia, Y. Wu, S. T. Nguyen and R. S. Ruoff, *Carbon*, 2007, **45**, 1558–1565.

64 V. C. Tung, M. J. Allen, Y. Yang and R. B. Kaner, *Nat. Nanotechnol.*, 2008, **4**, 25–29.

65 A. Wang, H. Wang, S. Zhang, C. Mao, J. Song, H. Niu, B. Jin and Y. Tian, *Appl. Surf. Sci.*, 2013, **282**, 704–708.

66 Q. Wang, L. Jiao, H. Du, Y. Si, Y. Wang and H. Yuan, *J. Mater. Chem.*, 2012, **22**, 21387–21391.

67 (*a*) J. W. Lee, T. Ahn, D. Soundarararajan, J. M. Ko and J.-D. Kim, *Chem. Commun.*, 2011, **47**, 6305–6307; (*b*) J. Xu, K. Wang, S. Z. Zu, B. H. Han and Z. Wei, *ACS Nano*, 2010, **4**, 5019–5026.

68 J. M. Soler, E. Artacho, J. D. Gale, A. Garcia, J. Junquera, P. Ordejon and D. Sanchez-Portal, *J. Phys.: Condens. Matter*, 2002, **14**, 2745–2779.

69 Y. Li, K. Ye, K. Cheng, J. Yin, D. Cao and G. Wang, *J. Power Sources*, 2015, **274**, 943–950.

70 B. Wang, J. Park, D. Su, C. Wang, H. Ahn and G. Wang, *J. Mater. Chem.*, 2012, **22**, 15750–15756.

This journal is © The Royal Society of Chemistry 2015

J. Mater. Chem. A, 2015, **3**, 18874–18881 | **18881**